

# Challenges in estimating emissivity and surface temperature using flux tower measurements

Gitanjali Thakur<sup>1,\*</sup>, Stanislaus J. Schymanski<sup>1,\*</sup>, Kaniska Mallick<sup>1</sup>, Ivonne Trebs<sup>1</sup>, and Mauro Sulis<sup>1</sup>

<sup>1</sup>Luxembourg Institute of Science and Technology, ERIN, Belvaux, L-4422, Luxembourg

\*gitanjali.thakur@list.lu

\*stanislaus.schymanski@list.lu

## ABSTRACT

Land surface temperature (LST) is a preeminent state variable that controls the energy and water exchange between the Earth's surface and the atmosphere. At the landscape scale, LST is derived from thermal infrared radiance measured using space-borne radiometers. At the plot-scale, the flux tower recorded longwave radiation components are inverted to retrieve LST. Since the down-welling longwave component was not measured routinely until recently, only the up-welling longwave component is often used for the plot-scale LST retrieval. However, we hypothesize that ignoring reflected down-welling longwave radiation for plot-scale LST estimations may lead to substantial discrepancies compared to the approach including down-welling longwave radiation. This also has important implications for estimating the correct surface emissivity using flux tower measurements, which is needed for plot-scale LST retrievals. This study addresses in detail the consequence of omitting downwelling longwave radiation for LST and emissivity estimation. It uses observations at ten eddy covariance towers on different land cover types. We found that the LST values obtained using both up-welling and down-welling longwave radiation components (long equation) are 0.5 to 1.5K lower than estimates using only the up-welling longwave radiation components (short equation). Plot-scale emissivity was estimated using a fitting procedure based on observed sensible heat flux and estimated surface-to-air temperature difference. The emissivity obtained using the long equation was generally lower than if the short equation was used. We also quantified the uncertainty in plot-scale LST and emissivity estimates due to uncertainty in measured fluxes. We found that despite additional input data for the long equation, the uncertainty in plot-scale LST was not greater than if the short equation was used. Landscape-scale day-time LST obtained from satellite data (MODIS TERRA) were strongly correlated with our plot-scale estimates, but on average, higher by several Kelvin, regardless of the estimation method. For most sites, the correspondence between MODIS LST and plot-scale LST estimates increased significantly if plot-scale emissivity was used instead of the landscape scale emissivity obtained from satellite measurements. The results of this work have significant implications for the combined use of aerodynamic and radiometric measurements (which require plot-scale emissivity estimation) to understand the interactions and feedbacks between LST and surface-atmosphere exchange processes.

## Introduction

The effects of global change are reflected in land surface temperature (LST) anomalies and their interannual variability<sup>1</sup>. It controls the magnitude and variability of the surface energy balance (SEB) components and simultaneously gets modulated by the SEB partitioning<sup>2,3</sup>. LST contains imprints of surface moisture and is extremely sensitive to evaporative cooling, which makes it a preeminent variable for studying evaporation and surface-atmosphere exchange<sup>4-6</sup>. It directly affects the amount of emitted longwave radiation and influences the saturation vapor pressure at the surface that drives latent heat flux. Thus, the ecohydrological functioning and carbon-water coupling are largely controlled by the surface temperature of the soil-vegetation system<sup>7</sup>. The availability of an extensive network of eddy covariance measurements (FLUXNET) allows us to understand the interactions and feedbacks between the surface-atmosphere exchange processes such as evaporation, transpiration, and its control by the atmosphere and vegetation at the diurnal time scale. However, the unavailability of direct LST measurements at the same scale hinders a detailed understanding of the interactions and feedbacks between LST and surface-atmosphere exchange processes, which is of utmost importance to the climate modeling community. In the last two decades, plot-scale radiometric data collected at eddy covariance sites (ECS) have gained popularity for in-situ LST retrieval due to its wide availability and high temporal resolution<sup>11,12</sup>. In addition to this, the LST estimates at plot-scale originate from a relatively homogeneous footprint in comparison to the satellite-derived LST (MODIS pixels). ECS measurements are primarily used to assess the impacts and feedbacks of climate change on key ecosystem fluxes<sup>13</sup>. By definition, LST is a thermodynamic

temperature that can be felt or measured by an accurate thermometer at the land surface-atmosphere point-of-contact and is independent of wavelength<sup>14</sup>. The instantaneous value of LST is the result of interplay between the net radiation at the surface, ground heat flux ( $G$ ), sensible heat flux ( $H$ ) and latent heat flux ( $LE$ )<sup>15</sup>. Thus, LST can also be used for the estimation of  $H$ <sup>16</sup> and  $LE$ <sup>17</sup> between the surface and the atmosphere. LST provides the lower-boundary condition in SEB models for diagnostic estimates of  $LE$  and is highly relevant for drought monitoring<sup>2,5,18</sup>. Inversion of the longwave radiation in FLUXNET data to obtain LST has been found to strongly depend on the emissivity of the underlying surface<sup>8</sup>, which is not available as routine measurement. Therefore, estimating in-situ LST is not straightforward due to the involvement of two unknowns (LST and emissivity) inside one measurement variable (up-welling longwave radiation). To circumvent this challenge, we conducted simultaneous retrievals of LST and emissivity by exploiting the longwave radiation components in conjunction with associated SEB flux measurements.

The SEB components can be sub-divided into radiative components (often lumped in net radiation,  $R_{net}$ ) and thermodynamic components, including sensible, latent and ground heat flux ( $H$ ,  $LE$ ,  $G$  respectively):

$$R_{net} = H + LE + G \quad (1)$$

As the surface-to-air temperature difference drives the exchange of sensible heat between surface and atmosphere, all components of Eq. (1) depend on the LST. Net radiation ( $R_{net}$ ) can be sub-divided into down-welling and up-welling components. Only a fraction of solar top-of-the-atmosphere radiation reaches the Earth's surface, as some is reflected back to space by clouds, some is absorbed by the atmosphere and emitted later as longwave radiation. The emitted longwave radiation as a function of surface temperature ( $T_s$ , K) and surface emissivity ( $\epsilon$ ) is given by Stefan-Boltzmann (SB) equation:

$$R_{lem} = \epsilon \sigma T_s^4 \quad (2)$$

where  $\sigma$  ( $\text{W m}^{-2}\text{K}^{-4}$ ) is the SB constant,  $\epsilon$  is the surface emissivity ranging between 0 and 1, and  $T_s$  (K) is the LST. Emissivity is defined as efficiency of a surface to emit thermal energy relative to a perfect black body. For a land surface, it depends on soil type, vegetation cover, soil moisture, soil chemistry, roughness, spectral wavelength, temperature and view angle<sup>9</sup>. Putting the radiative components together, we can sub-divide  $R_{net}$  into:

$$R_{net} = R_{sdwn} + R_{ldwn} - R_{sref} - R_{lref} - R_{lem} \quad (3)$$

Reflected shortwave in Eq. (3) is expressed as  $R_{sref} = \alpha R_{sdwn}$ , where  $\alpha$  is the surface albedo. Considering Kirchhoff's law, whereby the emissivity of a surface equals its absorptivity, emissivity values below unity result in reflected longwave radiation, expressed as:

$$R_{lref} = (1 - \epsilon) R_{ldwn} \quad (4)$$

LST or radiometric temperature is the “ensemble directional radiometric surface temperature”<sup>9</sup>, and can be estimated from the infrared radiance emanating from a given surface with known emissivity<sup>10</sup>. The emitted and down-welling longwave radiance are measured at given angle within its instantaneous field of view (fov) by a downward facing sensor relatively close to the surface (a few meters for an eddy covariance tower). The radiation received by a pyrgeometer or infrared sensor is a combination of the radiation emitted and reflected by the surfaces in its fov.

$$R_{lup} = R_{lem} + R_{lref} \quad (5)$$

Substitution of Eqs. (4 and 2) into Eq. (5) yields  $R_{lup}$  as a function of emissivity, surface temperature and down-welling longwave radiation:

$$R_{lup} = \epsilon \sigma T_s^4 + (1 - \epsilon) R_{ldwn} \quad (6)$$

Eq. (6) is then solved for LST as a function of measured longwave and known surface emissivity:

$$T_s = \sqrt[4]{\frac{R_{ldwn}}{\sigma} - \frac{R_{ldwn}}{\epsilon \sigma} + \frac{R_{lup}}{\epsilon \sigma}} \quad (7)$$

In order to invert LST as shown in Eq. (7),  $\epsilon$  values are required. However, radiometers at ECS do not measure spectral bands separately to deduce emissivity directly. Therefore, we will deduce  $\epsilon$  from observations of sensible heat flux ( $H$ ), which is defined as the heat transfer driven by a surface-to-air temperature difference. It can be expressed mathematically in analogy to Ohm's law as:

$$H = \rho C_p (T_s - T_a) / r_a \quad (8)$$

where  $T_a$  (K) is the temperature of the air measured at a reference height above the surface,  $C_p$  ( $\text{J kg}^{-1} \text{K}^{-1}$ ) is the specific heat capacity of air,  $\rho$  ( $\text{kg m}^{-3}$ ) is the air-density, and  $r_a$  ( $\text{s m}^{-1}$ ) is the total resistance to heat transport from surface to the atmosphere. In simplified form, we write:

$$H = m(T_s - T_a) \quad (9)$$

where  $m$  ( $\text{m s}^{-1}$ ) is a proportionality constant (defined as  $m = \rho C_p / r_a$  and broadly referred to as heat transfer coefficient) and depends on surface characteristics and micro-meteorology<sup>19</sup>. It is evident from Eq. (9) that for  $T_s - T_a = 0$ ,  $H$  will be zero. This boundary condition and the linear relationship between  $H$  and  $\Delta T$  has been used in the past to estimate  $\varepsilon$  at the plot-scale from observed  $H$ ,  $T_a$  and estimated  $T_s$  using measured longwave radiation<sup>20,21</sup>. Another approach for plot-scale  $\varepsilon$  estimation filters the data where  $H$  is close to zero, substitutes  $T_s$  in Eq. (6) by  $T_a$  and solves for  $\varepsilon$ <sup>22</sup>.

However, due to surface heterogeneity, sparse canopies are prone to footprint mismatch between the aerodynamic (flux tower) footprint and radiometric (hemispherical) footprint<sup>23–25</sup>, where the aerodynamic footprint represents the area contributing to measured sensible heat and air temperature, while the hemispherical footprint is the area within the radiometer footprint, contributing to the measured longwave radiation (used for  $T_s$  estimation). This can result in a different boundary condition i.e. at  $\Delta T = 0$ ,  $H \neq 0$  as expressed in Eq. (10):

$$H = m(T_s - T_a) \pm c(H) \quad (10)$$

where  $H$  is representative of the sensible heat flux from the eddy covariance tower footprint,  $T_s$  is representative of all the radiating surfaces in the radiometric sensor's view, and  $c$  is interpreted as the  $H$  from surfaces in the aerodynamic footprint that are not seen by the radiometer.

Plot-scale estimation of  $\varepsilon$  and LST using observed  $H$ ,  $T_a$ ,  $R_{lup}$  and  $R_{ldw}$  as described above and in the Methods section, may be prone to substantial uncertainty. It is unclear how uncertainties in observed fluxes propagate into the uncertainty of estimated LST and  $\varepsilon$ . By design, infrared thermal (IRT) sensors only measure up-welling infrared radiance and therefore cannot explicitly account for the amount of reflected down-welling infrared radiation in the signal. For a long time, down-welling longwave  $R_{ldw}$  was not routinely observed at ECS<sup>26</sup> and was also considered to be the most poorly quantified component of the radiation budget<sup>27</sup>. Therefore, the second term in Eq. (6) is commonly omitted, arguing that  $\varepsilon \approx 1$ , and therefore Eq. (6) is simplified to Eq. (2)<sup>28</sup>:

$$R_{lup} \approx \varepsilon \sigma T_s^4 \quad (11)$$

Eq. (11) can be solved for  $T_s$  to yield what we will term the "short equation" (seq) for  $T_s$ :

$$T_s \approx \sqrt[4]{\frac{R_{lup}}{\varepsilon \sigma}} \quad (12)$$

Note that the above derivation is actually flawed, as the second term of Eq. (6) was omitted arguing that  $\varepsilon \approx 1$ , and yet  $\varepsilon$  was retained in the first part of the equation. Nevertheless, even with the availability of down-welling longwave measurements<sup>29</sup>, the use of Eq. (11) is still a common practice<sup>8,30</sup>. This gives rise to the question if the short equation (Eq. 12) is adequate to estimate LST from ground-based measurements. In the remainder of this paper, we will refer to LST obtained using the long equation (Eq. 7) as  $T_{leq}$  and to LST obtained using the short equation (Eq. 12) as  $T_{seq}$ .

To better understand and improve approaches of plot-scale LST estimation, the present study addresses the following research questions:

1. Can we obtain an adequate estimate of plot-scale LST while neglecting the reflected down-welling longwave radiation?
2. Does the estimation of plot-scale  $\varepsilon$  based on observed sensible heat flux ( $H$ ) have an advantage over satellite-derived  $\varepsilon$  for plot-scale LST estimation?
3. How much uncertainty is introduced in plot-scale LST and  $\varepsilon$  due to uncertainty in measured EC fluxes?

To answer these questions, we analysed data for ten eddy covariance sites in different biomes and climates (see Table 2). Plot-scale broadband monthly emissivity was derived using observed  $H$  and estimated  $\Delta T$  as proposed by Holmes et al.<sup>20</sup>. Plot-scale LST was estimated using plot-scale or landscape scale emissivity with (Eq. 7) and (Eq. 12). Plot-scale LST was compared with MODIS LST (TERRA satellite-sensed) for the times of satellite overpass. Uncertainty in  $\varepsilon$  and LST due to uncertainty in observed fluxes were calculated using SOBOL based uncertainty analysis (SALib)<sup>31</sup>. See the Methods section for more details.

# 1 Results

## 1.1 Plot-scale $\epsilon$ using long and short equation

Following the method proposed by Holmes et al.<sup>20,32</sup>, plot-scale monthly  $\epsilon$  was estimated at the study site by fitting  $\epsilon$  to minimise the root mean square error (RMSE) of the regression between  $H$  and  $T_s - T_a$  (SI Fig. 11). In Fig. 1a, c, and d, we reproduced the original data of Figs. 2a, 3C, and 3Q from Holmes et al. (2009)<sup>20</sup> to validate our interpretation of their approach using the short equation (Eq. 12). We noted only marginal differences between the two results based on the short equation, which are likely due to different fitting algorithms. The replication of the  $H(\Delta T)$  plot using the long equation (Eq. 7) with the same data is given in Fig. 1b and the time series of resulting  $\epsilon$  values is shown in Fig. 1c, d, indicated by blue stars. The retrieved LST values were slightly higher when using Eq. (7) (compare a and b in Fig. 1). The use of the long equation (Eq. 7) resulted in substantially (10%) lower values of  $\epsilon$  as compared to the values estimated by Holmes et al.<sup>20</sup> for the common study sites (Brookings, Fig. 1c and Yatir, Fig. 1d).

Another approach for plot-scale  $\epsilon$  estimation (Maes et al. (2019)<sup>22</sup>) in combination with Eq. 7) resulted in even lower  $\epsilon$  values for Brookings, as shown in Fig. 1c (red stars), whereas at Yatir, this approach gave an  $\epsilon$  value higher than 1 (red star in Fig. 1d). Note that the long equation also yielded  $H(\Delta T)$  relationship for many more months at Yatir Forest (blue star) than the short equation (black dots) as shown in Fig. 1d, as it resulted in achieving a strong correlation between  $H$  and  $\Delta T$  (section 3 for details). The pattern of lower  $\epsilon$  and higher LST using the long equation compared to the short equation was confirmed for all the ten sites used in the present study (Table SI 2).

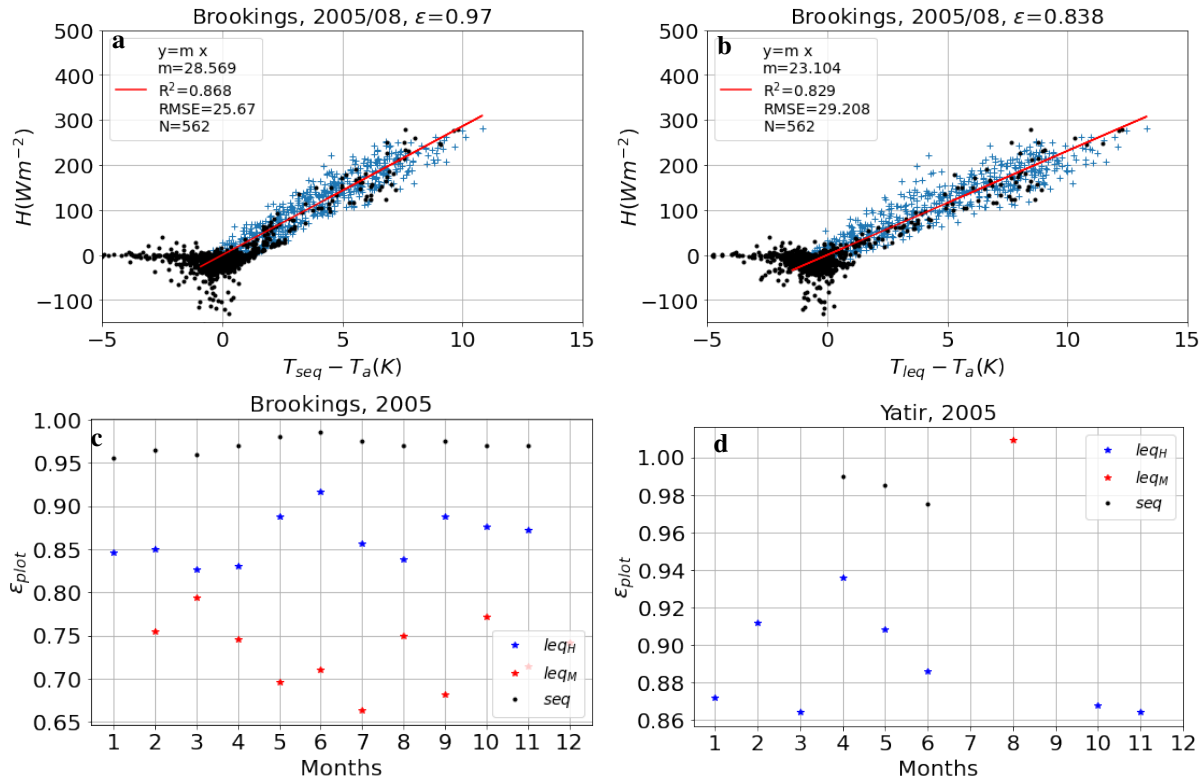


**Figure 1.** Reproduction of analysis presented in Figs. 2a, 3C, and Q in Holmes et al. (2009)<sup>20</sup>. (a) Sensible heat ( $H$ ) vs.  $\Delta T = T_{seq} - T_a$  based on the short equation ( $T_{seq}$ , Eq. 12); (b)  $H$  vs.  $\Delta T$  based on the long equation ( $T_{leq}$ , Eq. 7). Both show data for August 2005 at Brookings. Blue crosses represent data points satisfying the filtering criteria, while black dots represent points not considered in the analysis.  $N$  is the number of blue crosses used for regression (red line),  $m$  is the slope of regression,  $RMSE$  is the root mean square error and  $R^2$  is the square of the coefficient of determination. The fitted  $\epsilon$  value is reported in the title. (c) Optimised  $\epsilon$  values at Brookings obtained for the months where  $R^2 > 0.5$  using the short equation (Eq. 11, black dots) and long equation (Eq. 6, blue stars), and  $\epsilon$  obtained using the approach of Maes et. al (2019)<sup>22</sup> (red stars). (d) Same as (c), but for Yatir Forest, see table 2 for site descriptions.

## 1.2 Landscape scale vs plot-scale estimates of $\epsilon$ and LST

At each site, LST was estimated using both the short equation ( $T_{seq}$ , Eq. 12) and the long equation ( $T_{leq}$ , Eq. 7). In the first step, tower-based longwave radiation and landscape scale broadband  $\epsilon$  from MODIS spectral  $\epsilon$  ( $\epsilon_{MODIS}$ , Eq. 14) was used.

The yearly daytime surface-to-air temperature difference for each study site is estimated and shown in Fig. 2. At all sites, Eq. (12) resulted in higher day-time plot-scale  $T_s$  estimates as compared to Eq. (7), when using  $\epsilon_{MODIS}$ , with the medians of surface-to-air temperature differences ( $\Delta T$ ) differing by 0.8 to 1.5 K (Fig. 2). The difference in  $\Delta T$  using the two equations is highest at the water limited sites, e.g. AS and YA. Note that for two sites (LF and HS), the median values of daytime  $\Delta T$  are negative. Comparison of estimated plot-scale LST using  $\epsilon_{MODIS}$  at satellite overpass time with landscape scale LST ( $T_{MODIS}$ )

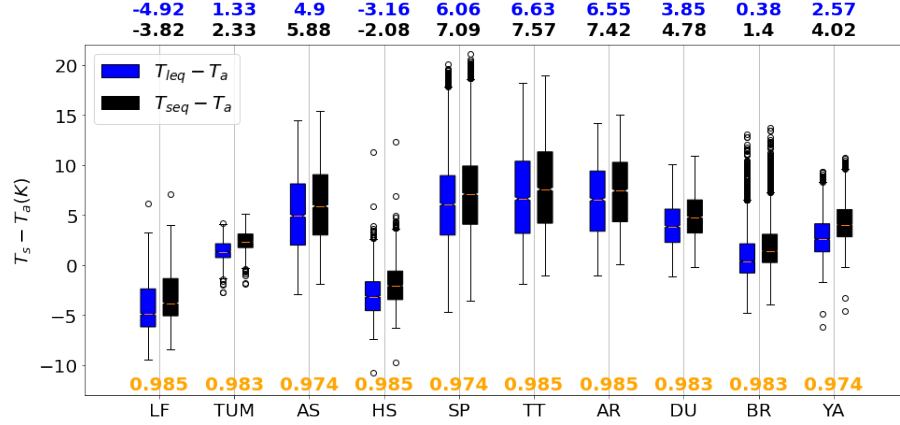


**Figure 2.** Yearly distributions of half-hourly surface-to-air temperature differences ( $\Delta T = T_s - T_a$ ) for a representative year at each site. LST was calculated using the short or long equation (Eq. 12, Eq. 7) with landscape-scale emissivity ( $\epsilon_{MODIS}$ ). The median values of  $\Delta T$  are shown at the top of the plot and the emissivities used for the  $T_s$  retrieval are shown at the bottom in orange. See Table 2 for site abbreviations.

revealed strong correlations between plot-scale and landscape scale LST estimates but systematically lower plot-scale LST (Fig. 3a, b). Use of plot-scale  $\epsilon_{plot}$  for LST estimation ( $T_{seq}$  and  $T_{leq}$ ) resulted in substantial reduction of the bias as shown in Fig. 3c, d. This trend in bias reduction was similar at other sites (Table SI2 for details). The minimum bias is found at TUM, a closed canopy (eucalypt forest) and the highest bias was obtained at LF and HS, heterogeneous ecosystems with sparse canopies (woodland savanna). However, for some sites, weak correlation between satellite-derived and local LST estimates were also evident (at DU,  $R^2$  was reduced from 0.8 to 0.4, see Table SI2). Also, using plot-scale  $\epsilon$  for LST estimation resulted in positive  $T_s - T_a$  at LF and HS as shown in SI3, Fig. 8 in comparison to Fig. 2.

### 1.3 Plot-scale $\epsilon$ estimation considering intercept

In order to account for the possibility of bias between radiometric and aerodynamic measurements (e.g. due to footprint mismatch of measuring devices or instrument bias) we also fitted Eq. 10, i.e. a relationship allowing for an intercept in the linear fit between  $H$  and  $\Delta T$  (instead of forcing it through zero as in Fig. 1) for plot-scale  $\epsilon$  estimation. As shown in Fig. 4, the plot-scale  $\epsilon$  values resulting from this approach ( $H = m \times \Delta T + c$ ) were substantially closer to the landscape-scale  $\epsilon$  values compared with the approach without intercept ( $H = m \times \Delta T$ ), as shown in Table (1). The resulting intercept values ranged from -24 to +258  $W m^{-2}$ , i.e. up to 70% of the maximum observed sensible heat flux at a site (e.g. at HS and TUM). Note, however, that if we assume just a slight under-estimation of upwelling longwave radiation by 40  $W m^{-2}$  (approx 8% of observed  $R_{lup}$ ), the intercept at HS was reduced from 237 to 17  $W m^{-2}$  (Fig. 5a). In this study, we did not apply any energy balance closure scheme, as a Bowen ratio closure resulted in even greater intercept values (Fig. 5b). The comparison of the resulting plot-scale LST with landscape scale LST values reveals an increase in bias at most sites compared to the LST obtained using  $\epsilon$  without an intercept, as shown in Table (1).

### 1.4 Uncertainty in plot-scale $\epsilon$ and LST

Each of the observed input variables used for the estimation of plot-scale  $\epsilon$  and LST has a certain level of measurement uncertainty associated with it. Here we present exemplary results for Alice Springs, which showed the highest correlation between plot-scale and landscape scale LST estimations (Table SI2). The uncertainty in plot-scale  $\epsilon$  estimated using Eq. (7) without allowing an intercept for  $H(\Delta T)$  ranged between 0.68 and 0.98. The short equation (Eq. 12) resulted in constrained values between 0.94 and 0.99 shown by the black boxes (Fig. 6a). The uncertainty in  $\epsilon$  is propagated to obtain hourly uncertainty in  $T_s - T_a$  using Eq. (7) and Eq. (12) as shown in Fig. 6b, c. The uncertainty range for plot-scale LST was quite similar for both long and short equation (blue and black boxes in Fig. 6b, c). The uncertainty in  $T_s - T_a$  increased when landscape-scale  $\epsilon$  was used as shown by the orange boxes in Fig. 6b, c.





**Figure 3.** Landscape scale LST ( $T_{MODIS}$  derived from MOD11A1) vs. plot-scale LST at Alice Springs for 2016-2018. **(a)**  $T_{seq}$  based on short equation (Eq. 12) and satellite-derived (MODIS) broadband emissivity; **(b)** Same as (a), but  $T_{leq}$  based on long equation (Eq. 7); **(c)**  $T_{seq}$  based on short equation (Eq. 12) and monthly plot-scale emissivity; **(d)** Same as (c), but  $T_{leq}$  based on long equation (Eq. 7). Bias is mean  $T_{seq} - T_{MODIS}$ ,  $N$  is the number of daily overpasses of MODIS between 2016 and 2018,  $c$  is the intercept,  $m$  the slope, RMSE is the root mean square error and  $R^2$  is coefficient of determination. At each site, LST was estimated using both the short equation ( $T_{seq}$ , Eq. 12) and the long equation ( $T_{leq}$ , Eq. 7). In a first step, we used satellite-derived landscape scale broadband emissivity from MODIS ( $\epsilon_{MODIS}$ , Eq. 14) for estimating plot-scale LST from tower-based longwave measurements, and compared these with landscape-scale LST extracted from MODIS LST dataset ( $T_{MODIS}$ )

## 2 Discussion

Our analysis revealed the deficiency in commonly used short equation for estimating plot-scale LST and  $\epsilon$ . The use of long equation for plot-scale  $\epsilon$  estimation results in lower values for canopy with heterogeneous land cover. In order to obtain realistic  $\epsilon$  for sparse canopy with heterogeneous landcover, acknowledging footprint mismatch between radiometric and aerodynamic measurements becomes important.

Depending on the equation (Eq. 7 or Eq. 12) used to estimate LST, a small approximation (error) in  $\epsilon$  can lead to a large error in LST (SI Fig. 10). The sensitivity of the long equation (Eq. 7) to  $\epsilon$  is driven by the contrast between  $R_{lup}$  and  $R_{ldwn}$  whereas, for short equation (Eq. 12), it is only driven by observed  $R_{lup}$  (SI Fig. 9). For instance, an error of 0.01 in  $\epsilon$  at water limited sites like AS can cause an error of 0.17K using Eq. (7) and 0.79K using Eq. (12) respectively (SI Fig. 10). This shows a clear advantage of using Eq. (7) for plot-scale LST estimation, since, plot-scale  $\epsilon$  is unknown and therefore used as an approximate value<sup>8</sup>. Also, plot-scale  $\epsilon$  estimation using long equation (Eq. 7) results into  $H(\Delta T)$  relationship for more months ( $R^2 > 0.5$ , blue stars in Fig. 1d). However,  $\epsilon$  estimates using Eq. (7) are lower than Eq. (12) and in particular for sites like HS and LF, the  $\epsilon$  was unrealistic (SI Table 4) in comparison to the previously reported  $\epsilon$  values for a soil-vegetation system<sup>33,34</sup>.

The lower  $\epsilon$  value using long equation for sparse canopy (Table 1) suggests bias due to combining measurements coming from instruments (radiometer, eddy covariance system) characterized by different footprints<sup>24</sup>. The mismatch of source areas becomes important if the surface underlying the instruments have heterogeneous land cover (e.g. AS, TT, YA, AS, HS, LF). However, "footprint awareness" is often omitted at ECS under the assumption of homogeneity<sup>23</sup>. The mismatch in footprint can result in unrepresentativeness of the targeted ecosystem which may further lead to  $H \neq 0$  at  $\Delta T = 0$ . This problem was not detected by Holmes et al.<sup>35</sup>, as the short equation (Eq. 12) was used, and due to its high sensitivity to  $\epsilon$  (SI Fig. 10 a) even

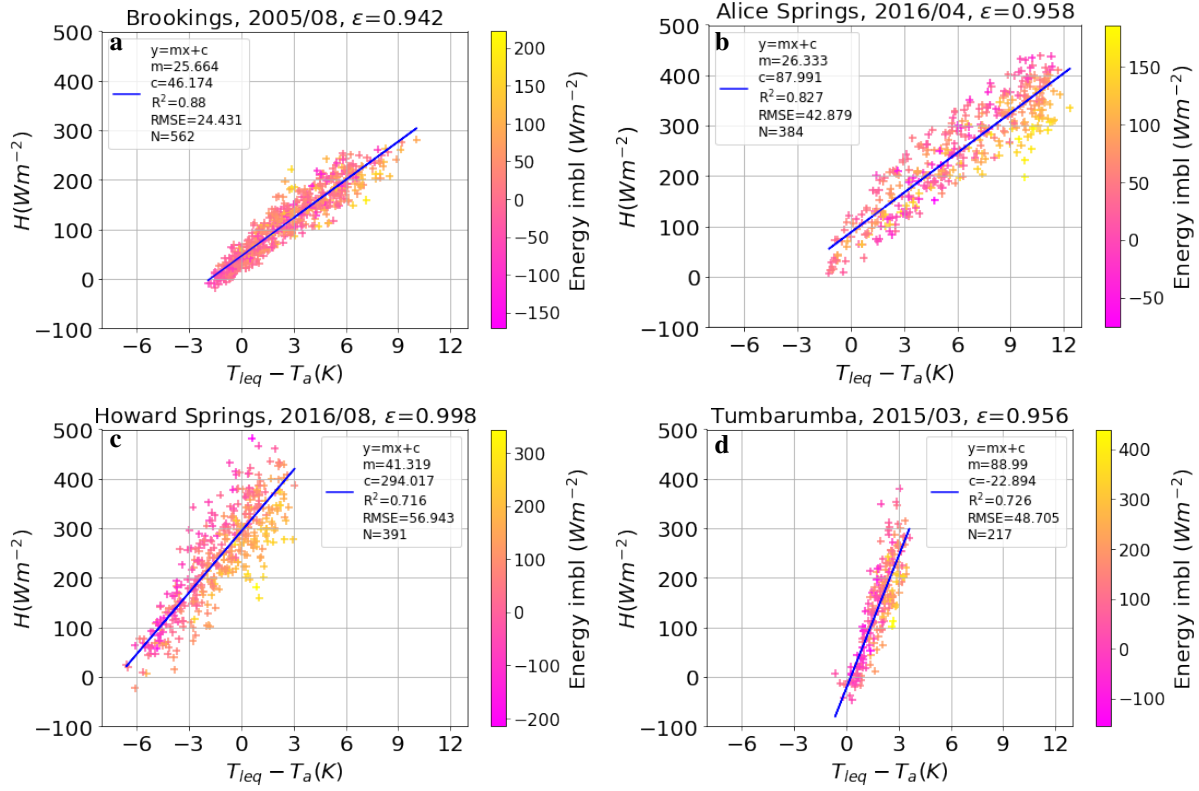


**Figure 4.** Sensible heat flux as a function of surface-to-air temperature difference based on Eq. 10 ( $H = m(T_s - T_a) + c$ ).  $\varepsilon$  was fitted to minimise RMSE of a robust linear regression. The title of the plot contains site, year, month and the fitted  $\varepsilon$ -value. The legend correspond to Fig. 1. The colour code indicates the degree of energy imbalance of each data point (i.e.  $R_{\text{net}} - H - LE - G$ ).

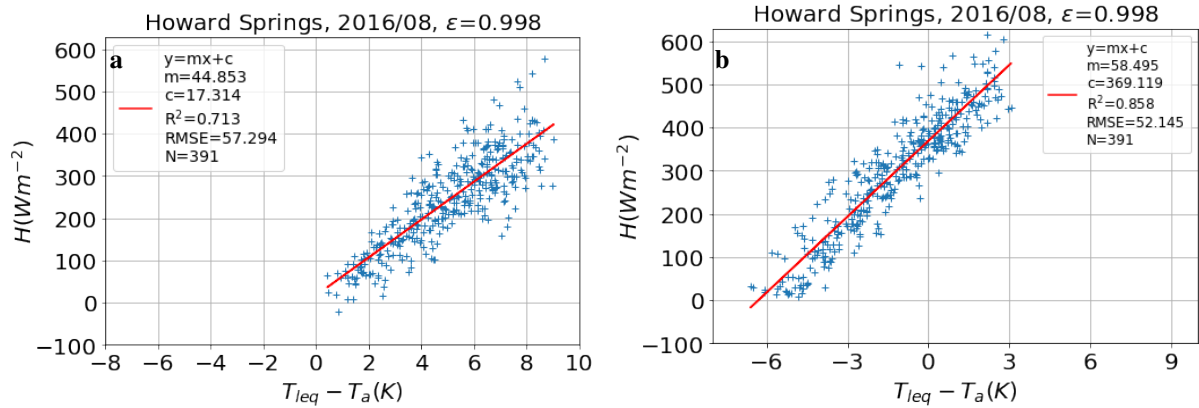


**Figure 5.** Sensible heat flux as a function of surface-to-air temperature difference based on Eq. 10 ( $H = m(T_s - T_a) + c$ ). Same analysis and legends as in Fig. 4(c), but (a) After adding  $40 \text{ (Wm}^{-2}\text{)}$  to measured  $R_{\text{lup}}$ , and (b) after closing the energy imbalance using a Bowen ratio closure scheme.

with small reduction in  $\varepsilon$  the offset in  $H(\Delta T)$  was corrected (Fig. 1a). Whereas, due to lower sensitivity of Eq. (7) to  $\varepsilon$  (SI Fig. 10 a), a larger reduction is required to remove the intercept resulting into lower  $\varepsilon$  as shown in Fig. 1b. We proposed an improvement to the method by allowing an intercept in  $H(\Delta T)$  regression (robust regression). Considering the aerodynamic footprint to be larger than the radiometric footprint<sup>23,24</sup>, the offset was interpreted as the  $H$  from the aerodynamic footprint which is not seen by the radiometer and resulted into realistic  $\varepsilon$  (Fig 4a, b, c, d). The intercept was very high for sites like HS and LF (Table. 1). Placing high value of intercept into perspective for HS and LF, we looked closely at  $H(\Delta T)$  plots for HS and LF (SI Fig. 8) and negative daytime  $T_s - T_a$  (Fig. 2) we could hypothesize an underestimation of  $R_{\text{lup}}$ . Testing the hypothesis for HS (having high intercept, Fig. 4c) we found that adding roughly  $40 \text{ Wm}^{-2}$  (approx 8% of observed  $R_{\text{lup}}$ , Fig.

Sites	Landscape-scale $\varepsilon$			Plot-scale $\varepsilon$ $H = m * (\Delta T)$			Plot-scale $\varepsilon$ $H = m * (\Delta T) + c$			
	$\varepsilon_{land}$	$R^2$	bias (K)	$\varepsilon_{plot}$	$R^2$	bias (K)	$\varepsilon_{plot}$	$R^2$	bias (K)	c ( $Wm^{-2}$ )
SP	0.974	0.81	-4.61	0.85	0.82	-1.91	0.92	0.774	-2.563	18.12
AS	0.974	0.93	-6.24	0.82	0.93	-1.92	0.993	0.915	-4.884	72.46
TT	0.974	0.57	-8.30	0.80	0.52	-4.02	0.939	0.521	-7.466	58.70
HS	0.985	0.16	-9.90	0.6	0.22	-2.47	0.949	0.18	-10.45	237.29
LF	0.985	0.41	-11.0	0.6	0.41	-2.57	0.968	0.378	-11.47	258
AR	0.985	0.27	-3.51	0.960	0.252	-2.98	0.996	0.27	-3.567	14.72
DU	0.985	0.81	4.61	0.985	0.425	-3.926	0.994	0.405	-4.603	-8.11
TUM	0.983	0.84	-2.10	0.97	0.89	-1.93	0.955	0.85	-1.696	-24.24
BR	0.983	0.937	-0.195	0.82	0.895	2.72	0.919	0.906	1.662	17.72
YA	0.974	0.855	-3.45	0.93	0.793	-0.582	0.873	0.826	0.073	-22.95

**Table 1.** Comparison of daytime landscape scale LST ( $T_{MODIS}$ ) with plot-scale LST ( $T_s$ ) estimated at TERRA time of pass using long equation. The emissivity used to retrieve plot-scale LST is derived using relationship without intercept and with intercept at the study sites are reported. The reported  $\epsilon_{plot}$  and intercept (c) are median values and landscape emissivity are MODIS based. Bias is defined as mean of  $T_s - T_{MODIS}$ ,  $R^2$  is coefficient of determination between plot-scale LST in comparison to landscape scale LST. The site acronyms can be found in Table 2.

12) in observed  $R_{lup}$  led to significant reduction in the intercept from  $294 Wm^{-2}$  (Fig. 4 c) to  $17 Wm^{-2}$  with positive  $T_s - T_a$  as shown in Fig. 5a. The other linear regression parameter m,  $R^2$ , RMSE remained constant for Fig. 5a and Fig. 4c. The hemispherical view of the radiometers looking down at the heterogeneous canopy, makes it possible to have more tree crowns and less soil for HS and LF. This can lead to an underestimation of  $R_{lup}$ , approximately by 5-10% (SI 6, Fig. 12). Also, the offset in  $H(\Delta T)$  was proportional to the maximum observed  $H$  for each month as shown in Fig. 4. The ratio between  $H_{max}$  and intercept varies between 0% to 30% for AS (SI 7 Fig. 13). Previous studies have shown the dependence of footprint mismatch on wind direction<sup>23-25</sup> however we did not find and significant relation between intercept and dominant wind direction for each month. Surface heterogeneity has also been recognized as one of the potential causes for the lack of energy balance closure observed at most ECS<sup>11,36</sup> at diurnal scales. Therefore, as a prerequisite the observed turbulent fluxes are corrected using an energy balance closure scheme<sup>37</sup> before use. However, in our analysis the use of an energy balance closure scheme (based on Bowen ratio) led to much lower values of plot-scale  $\epsilon$  using Holmes approach. Other studies on plot-scale  $\epsilon$  estimation have also used the observed fluxes without correction<sup>22,35,38,39</sup>. The use of an energy balance closure scheme for plot-scale  $\epsilon$  estimation led to an increase in positive intercept (sparse canopy, Fig. 4). We also looked into the intercept of  $H(\Delta T)$  by closing energy imbalance using Bowen ratio closure scheme<sup>37</sup> which result into higher intercept as shown in Fig 5b. These results show that the relation between intercept in  $H(\Delta T)$  and lack of energy balance closure is not conclusive.

Comparison of plot-scale LST with MODIS LST resulted into very high bias for sparse canopy which is in agreement with previous studies where the bias for sparse canopy reached upto  $12K$ <sup>40</sup>. Plot-scale LST estimates using plot-scale  $\epsilon$  reduced the bias in comparison to MODIS LST as shown in Table 4. The use of plot-scale  $\epsilon$  also reduces the uncertainty in diurnal LST in comparison to landscape scale  $\epsilon$  (Fig. 6b,c). However, LST estimated using plot-scale  $\epsilon$  considering foot print mismatch ( $H = m * \Delta T + c$ ) resulted into increase in bias for most of the study sites as shown in Table 1. The increase in bias could be attributed to implicit consideration of spatial heterogeneity (by accepting intercept) at plot-scale, whereas, MODIS LST (landscape scale) are integrated pixel information considering radiating signal from a homogeneous surface.

The fluxes observed at a soil-vegetation system is representative of the composite signal from both, soil and vegetation which typically have a different range of surface temperatures and emissivities<sup>41</sup>. The  $\epsilon$  of soil strongly depends on soil moisture content<sup>42</sup>, whereas, the  $\epsilon$  of a canopy depends on its structural attributes and leaf area index, the latter of which varies strongly at the seasonal scale<sup>43</sup>. For example, the laboratory-measured directional  $\epsilon$  for various canopy elements (bark, leaf and its arrangement, stem wood) ranged between 0.9 to 1<sup>44</sup>. Laboratory measurements of thermal infrared reflectance spectra suggests that the  $\epsilon$  variation from structural unknowns, such as leaf orientation, is more significant than the differences in leaf component emissivity among plant species<sup>34</sup>. Consequently, it is clear that the  $\epsilon$  of a surface is a function of many factors and detailed study of all these factors is out of scope of the present study. Thus, derivation of landscape-scale broadband  $\epsilon_{land}$  from narrowband spectral emissivity is considered as a first-order approximation for capturing the integrated effects of land cover from MODIS spectral bands<sup>41</sup>. However, due to general lack of emissivity information for natural ecosystem at ECS, satellite derived emissivity serves as plausible estimates and are valuable input for plot-scale LST estimation. Plot-scale  $\epsilon$  by fitting observed  $H$  and estimated  $\Delta T$  without an intercept results into a lower value and is statistically questionable<sup>45</sup>. Since fluxes



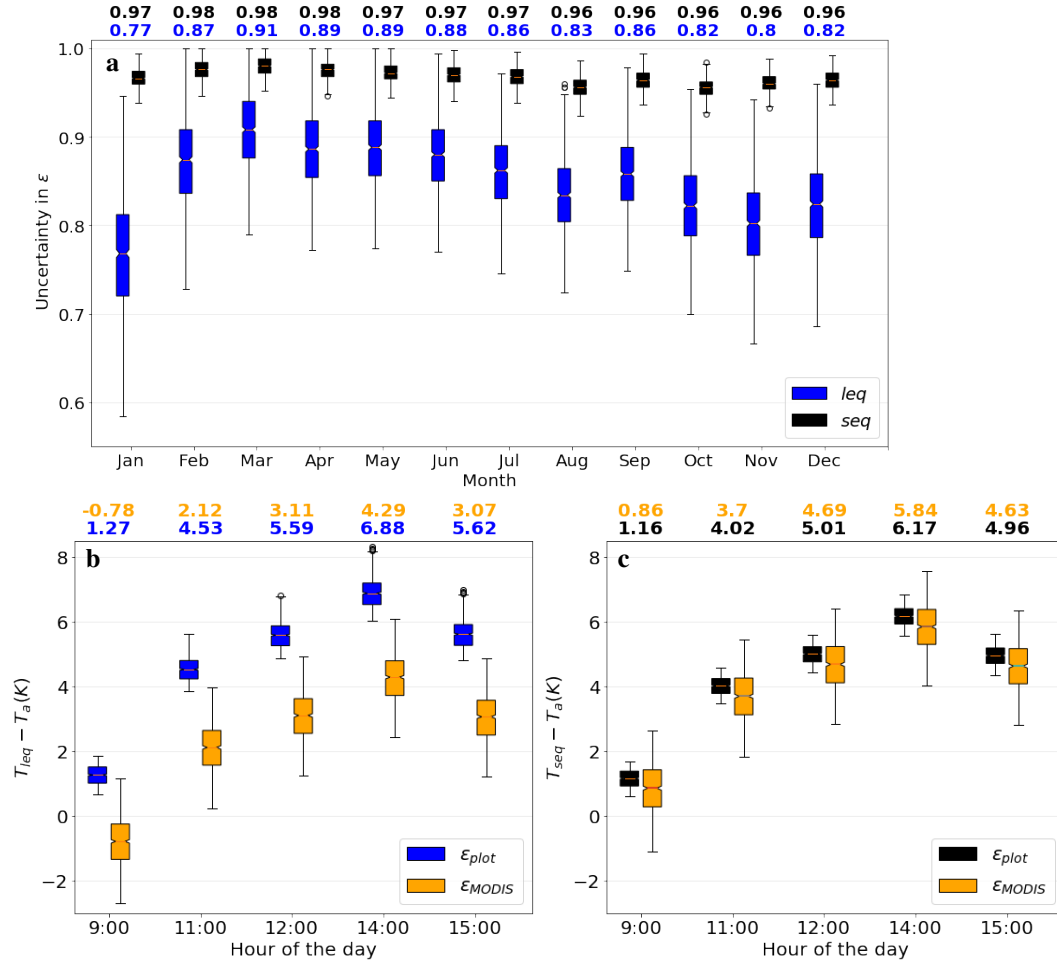


**Figure 6.** Uncertainty in monthly plot-scale  $\epsilon$  exemplarily for 2017 and hourly  $T_s - T_a$  for 15 August 2017. (a) Uncertainty in monthly optimised emissivity due to uncertainty in  $H, R_{lup}, R_{ldw}, T_a$  at using Eq. (6) and Eq. (11) shown in Blue and black for 2017 at AS. (b) Hourly daytime uncertainty in  $T_s - T_a$  due to perturbed (observed + measurement uncertainty) fluxes and optimum  $\epsilon$  using Eq. (6) in blue. Perturbed fluxes with MODIS based  $\epsilon$  in orange (Fig. (2)). (c) Hourly daytime uncertainty in  $T_s - T_a$  due to perturbed fluxes and optimum  $\epsilon$  using Eq. (11) in black and perturbed fluxes with MODIS  $\epsilon$  in orange. Optimum  $\epsilon$  values calculated from observation (without adding uncertainty) and  $T_s - T_a$  values correspond to the median of perturbed values.

observed at ECS contain composite (soil and vegetation) signal aggregated over space and time therefore forcing  $H(\Delta T)$  linear fit through zero is a simplification. Accepting an intercept in  $H(\Delta T)$  linear regression gives a consistent slope to the curve which lead to reasonable representation of the observation at ECS further results into realistic range of  $\epsilon_{plot}$ . Estimation of an intrinsic property like  $\epsilon$  using time varying fluxes can be considered imprecise; however, considering the spatial and temporal limitation of satellite derived data, the plot-scale  $\epsilon$  estimation is a good alternative.

Our results show that under no condition for grey bodies, the use of short equation and long equation can lead to equal values of  $\epsilon$  and LST and thus, the use of Eq. (12) is not recommended. Considering the widely spread use of both ECS recorded fluxes and MODIS LST in LSMs applications, the use of plot-scale  $\epsilon$  can be advantageous as it reduces the bias between plot-scale and MODIS LST. Plot-scale  $\epsilon$  also lowers the uncertainty in diurnal LST due to measurement uncertainty in comparison to the MODIS based emissivity. Therefore, the approach proposed in this work has the potential to provide a more robust benchmark information for model calibration and validation. Realistic estimate of plot-scale  $\epsilon$  by allowing an intercept in the linearfit of  $H(\Delta T)$  emphasises on integration of "footprint awareness" concept for using eddy covariance fluxes. Overall, the implications of our study are of particular relevance for the research community interested in understanding diurnal and seasonal feedback in soil-vegetation systems based on fluxes, emissivity and LST estimated at a consistent scale.

### 3 Methods

#### 3.0.1 Research data

**Tower data:** ECS collect micro-meteorological measurements above the surface (vegetation canopy) using towers (flux tower) following common measurement protocols<sup>13</sup>. The towers are commonly equipped with an instrument made up of pyrgeometers or radiometers to measure up-welling and down-welling shortwave and longwave radiation, which is further used to calculate net radiation (Eq. 3). Besides radiative fluxes, measurement at ECS also include sensible and latent heat fluxes, net carbon-dioxide exchange and a range of meteorological variables, such as air temperature, humidity and wind speed.  $T_a$  is the air temperature measured at a reference height above the canopy. Each flux measurement is accompanied by a flagging system based on the second CarboEurope-IP QA/QC workshop<sup>46</sup>. Flag 0 is designated as high data quality, and have been used in our current work. For the analysis, ten sites were selected to represent a variety of land cover types and climates (Table 2). Eight sites belong to the North Australian Tropical Transect (NATT) and 2 sites (Yatir Forest, Brookings) are chosen to replicate results from Holmes et.al<sup>35</sup>. Eddy covariance Level 3 data is obtained from <http://data.ozflux.org.au/portal/pub/listPubCollections.jsp> for Australian sites. The data for Brookings was obtained from ameriflux whereas the data for Yatir Forest was obtained from personal communication with Professor Yakir's lab in order to obtain the older version of the data which was used by Holmes et al.<sup>20</sup>

**MODIS data:** Landscape scale emissivity and LST data (MODIS product MOD11A1) was downloaded from NASA earth data . It is a level 3 daily LST product gridded in the sinusoidal projection at a spatial resolution of 0.928 km by 0.928 km. The daily LST pixel values in each granules (tile contains 1200 x 1200 grids in 1200 rows and 1200 columns) is retrieved by the generalized split-window algorithm under clear-sky conditions and MODIS LST values are averaged by overlapping pixels in each grid with overlapping areas as weight<sup>47</sup>. The downloaded data in hierarchical data format (hdf), were converted into tagged image file format (tiff) using a python package called PyModis<sup>48</sup>. From tiff the files are converted into csv format. The details of data extraction and conversion can be found at <https://renkulab.io/projects/gitanjali.thakur/modisstatspar/>. The dataset columns used to compare plot-scale LST and emissivity are: day time daily LST, local view time, night view time, channel 31, 32 spectral  $\epsilon$  respectively.

**Site specific approach:** This approach was initially proposed by Holmes<sup>35</sup> to estimate plot-scale  $\epsilon$  using short equation with  $H$ ,  $R_{lup}$ ,  $T_a$ . In the present work, we have used both long equation (Eq. 7) and short equation (Eq. 12) to estimate  $\epsilon$ . The prime variable used in the study are  $H$ ,  $R_{lup}$ ,  $R_{ldwn}$ , and,  $T_a$  while the ancillary variables  $R_n$  and wind speed ( $W_s$ ) are used to filter the data for analysis. The filtering condition were ( $R_n > 25Wm^{-2}$ ) and wind speed ( $W_s > 2ms^{-1}$ )<sup>20</sup>. Plot-scale emissivity is derived by segregating each month data satisfying the filtering criteria. For estimating  $T_s$  from longwave measurement ( $R_{lup}$ ,  $R_{ldwn}$ ), a predefined range of  $\epsilon$  is chosen starting from 0.998 and is reduced with a step-size of 0.002 upto 0.4. For each month data,  $H(T_s - T_a)$  linear regression is performed using scipy <https://docs.scipy.org/doc/scipy-0.14.0/reference/generated/scipy.stats.linregress.html>. The squared correlation coefficient ( $R^2$ ) is checked and months where  $R^2 > 0.5$  (i.e. substantial part of variance in  $H$  is explained by  $T_s - T_a$ ) is chosen for  $\epsilon$  estimation. To obtain  $\epsilon$ , the regression line of  $H(\Delta T)$  is forced through origin (at  $T_s - T_a = 0$   $H = 0$ ) by minimising the RMSE. An illustration plot for RMSE and  $\epsilon$  is shown in SI5. The  $\epsilon$  is obtained for each month using both, long Eq.(7) and short equation Eq.(12) and termed as  $\epsilon_{leq}$  and  $\epsilon_{seq}$  respectively, as shown in Fig. 7b.

In order to represent the observation to account for the role of spatial heterogeneity at ECS,  $H(\Delta T)$  linear fit is allowed to have an offset. The plot-scale  $\epsilon$  was obtained by minimising RMSE as explained before (an example for one month at AS in Fig. 11). Plot-scale LST estimated using plot-scale  $\epsilon$  (with and without intercept in  $H(\Delta T)$  linear fit was compared to landscape scale MODIS LST. Monthly tower-based longwave measurement at study sites corresponding to TERRA daily time of pass was obtained using linear interpolation. TERRA (satellite) overpasses at local solar time between 10:30 am to 12 pm in ascending mode<sup>14</sup>. Plot-scale LST at local satellite overpass ( $T_{leq}$  and  $T_{seq}$ ) was obtained using interpolated longwave radiation measurement and coresponding monthly plot-scale  $\epsilon$ . Plot-scale daily LST is compared to MODIS LST in terms of mean, bias, RMSE and  $R^2$  using a robust linear regression model (scipy stat model) as shown in Fig. 7a. The goodness of fit between plot-scale and landscape scale LST was determined by looking at  $R^2$  as shown in Fig. 7b. The bias is estimated as mean of deviation between daily MODIS LST and ground based  $T_s$  ( $T_{leq,seq} - T_{MODIS}$ ). See SI table for data sources and acronyms in SI1.

The other approach for plot-scale  $\epsilon$  estimation using Eq. (5) is discussed by Maes et.al (2019)<sup>22</sup>. For each month, the observed  $R_{lup}$ ,  $R_{ldwn}$ ,  $T_a$  are filtered for non rainy days,  $-2 < H < 2$ , and  $\alpha < 0.4$ . The  $\epsilon$  is estimated by substituting  $T_s = T_a$  in Eq. (5) as shown in Eq. (13). The monthly  $\epsilon$  was represented as the median of  $\epsilon$  obtained by substituting filtered data in Eq. (13).

$$\epsilon = \frac{R_{ldwn} - R_{lup}}{R_{ldwn} - T_a^4 \sigma} \quad (13)$$

**General approach:** The radiative energy emitted at a specific wavelength is related to its temperature using Planck's

**Table 2.** Description of study sites

Study site	latitude, longitude	Landcover	Time- period	longwave sensors	Sensor instal- lation height (m)
Sturt Plains (SP)	-17.1507, 133.3502	Mitchell Grass	2016- 2019	CG-2	4.8
Alice Springs (AS)	-22.2828, 133.2493	Mulga wood- land, hummock grassland, river red gum forest	2016- 2018	CNR1	12.2
Ti Tree East (TT)	-22.2870, 133.6400	Grassy mulga woodland, Corym- bia/Triodia savanna	2016- 2018	CNR1	9.9
Howard Springs (HS)	-12.4943, 131.1523	Open woodland savanna	2016- 2018	CM-7B, CG-2	23
Litchfield (LF)	-13.1790, 130.7945	Tropical sa- vanna	2016- 2018	CNR4	31
Adelaide River (AR)	-13.0769, 131.1178	Savanna domi- nated by Euca- lyptus tectifica and Planchonia careya	2006- 2009	CNR1	15
Daly Uncleared (DU)	-14.1592, 131.3881	Woodland savanna	2016- 2018	NRLite	21
Tumbarumba (TUM)	-35.6566, 148.1517	Wet sclerophyll	2015- 2018	CM3 and CG3	70
Brookings (BR)	44.352, 96.840	Cropland	2005	pyrgeometers <sup>14</sup>	NA
Yatir Forest (YF)	35.052, 31.345	Evergreen needleleaf forest	2005	pyrgeometers <sup>14</sup>	NA

function<sup>49</sup>. Thermal remote sensing (MODIS) is used to measure spectral emissivity through four channels (28, 29, 30, 31) at wavelengths ranging between 8-12  $\mu\text{m}$ <sup>41</sup> and the system of equations is iteratively solved for a given range of wavelengths (9 - 12 $\mu\text{m}$ ) to obtain  $\epsilon$  and LST using radiative transfer models<sup>50–52</sup>. We estimate landscape scale broadband  $\epsilon$  using MODIS spectral  $\epsilon$  as shown in Bahir et. al (2017)<sup>53</sup>.

$$\epsilon_{MODIS} = 0.4587\epsilon_{31} + 0.5414\epsilon_{32} \quad (14)$$

Tower based longwave radiation measurement ( $R_{lup}$ ,  $R_{ldwn}$ ) passing the filtering criteria (as mentioned in site specific approach) along with MODIS based  $\epsilon$  was used to invert LST using Eq. (7) and Eq. (12). The obtained plot-scale LST was compared to landscape scale MODIS LST using a robust linear regression as mentioned in site specific approach as shown in Fig. 7a.

**Uncertainty estimation:** The turbulent fluxes of  $H$  measured at the ECS are averaged over smaller time (30 or 60 minutes) and the averaging over this time interval is typically dominated by random errors<sup>54,55</sup>. The other source of error is the radiation measurement which can vary between sites due to the difference in accuracy and precision of the in-situ radiometers or pyrgeometer, differences in field of view (fov), wavelength bands, and spectral response functions of the sensors. For reference, the accuracy of dedicated infrared temperature (IRT) sensors is given by their manufacturers as 0.5K, but it is not clear what sources of uncertainty are considered in this estimation<sup>56</sup>. Thus, we estimated the uncertainty in plot-scale  $\epsilon$  due to uncertainty in observed fluxes. In a first step, the error bounds of each input variables ( $H$ ,  $R_{lup}$ ,  $R_{ldw}$ ,  $T_a$ ) used in plot-scale  $\epsilon$  is defined. The error bounds for  $R_{lup}$  and  $R_{ldwn}$  are -5 to 5  $\text{W m}^{-2}$ <sup>27</sup>, for  $H$ , it is -20 to 20  $\text{W m}^{-2}$  and for  $T_a$ , it is -1 to 1  $\text{K}$ <sup>37</sup>. Uniformly

distributed error samples within bounds is generated using saltelli sampling scheme<sup>57</sup> using python based package name SALIB. Each error samples is added to the monthly segregated measured fluxes as explained in site specific approach. The  $H(\Delta T)$  linear fit for the fluxes with added uncertainty (error sample) is obtained and plot-scale  $\epsilon$  is estimated by minimising RMSE as explained in site specific approach. The range of plot-scale  $\epsilon$  is reported as uncertainty in  $\epsilon$ . The plot-scale  $\epsilon$  uncertainty is propagated to obtain uncertainty in hourly LST using short equation Eq. (12) and long equation Eq. (7) as shown in Fig. 6b, c.

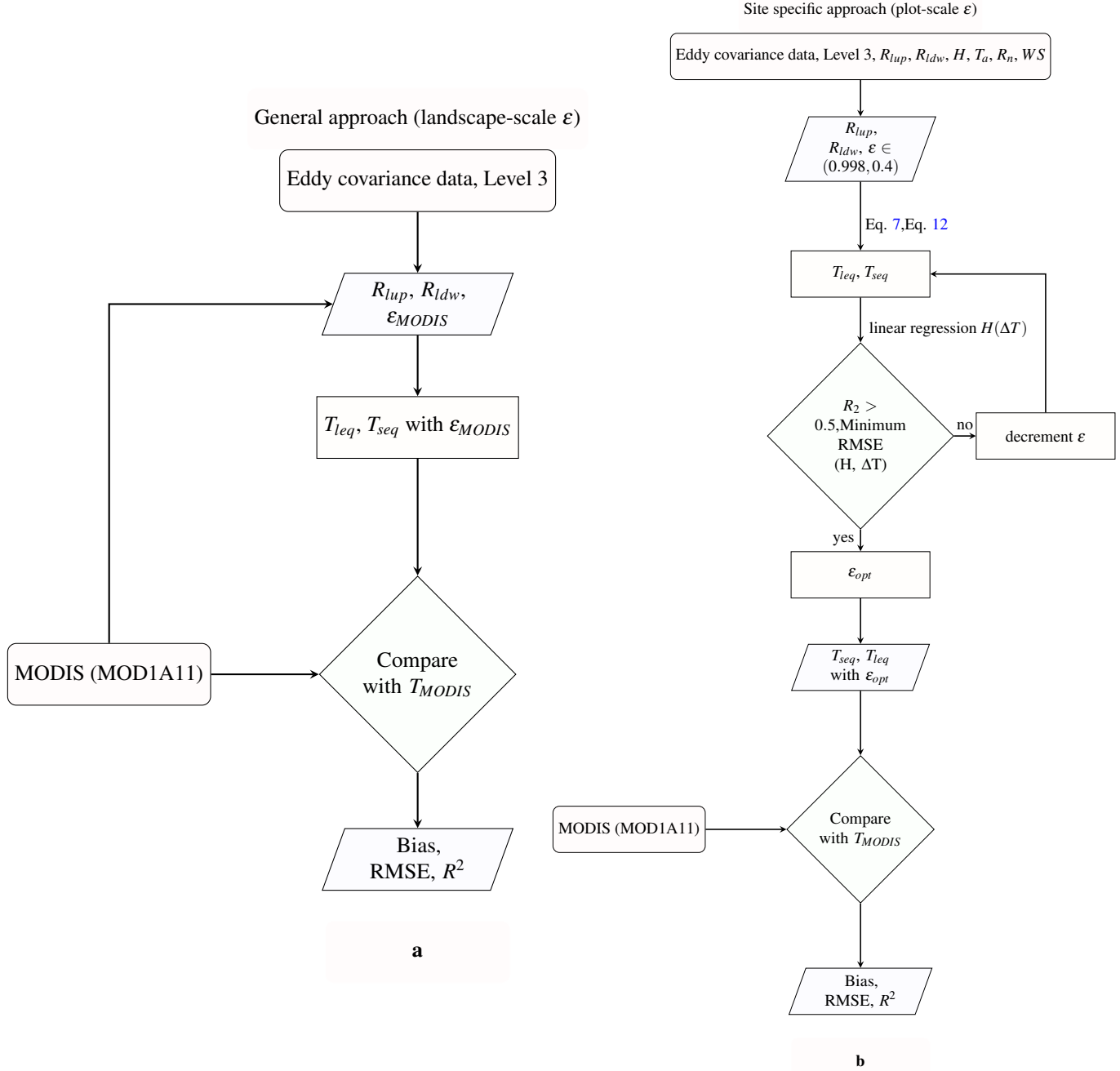


**Figure 7.** Schematic representation of steps followed for plot-scale LST retrieval using eddy covariance measurement (a) Landscape emissivity and longwave measurement and compared to Landscape-scale LST ( $T_{MODIS}$ ) (b) Plot-scale emissivity estimation using observed  $H$ ,  $R_{ldwn}$ ,  $R_{lup}$  and plot-scale LST is estimated using plot-scale  $\epsilon$  is compared to landscape-scale emissivity. The  $R^2$ , RMSE, Bias are mentioned in Fig. (3)

## 4 Acknowledgements

We would like to thank Dr. Maik Renner for pointing us to the work by Holmes et al. and Dan Yakir's lab for providing Yatir Forest data and helpful discussions. We are also grateful to Thomas Foken, Jason Beringer, Lindsay Hutley for insightful discussions and Remko Nijzink for his help in programming and RENKU. This work is supported by the Luxembourg National Research Fund (FNR) ATTRACT programme (WAVE, A16/SR/11254288). Mauro Sulis acknowledges the financial support of the FNR CORE programme (CAPACITY, C19/SR/13652816).

## References

1. Rowell, D. P. A scenario of european climate change for the late twenty-first century: seasonal means and interannual variability. *Clim. Dyn.* **25**, 837–849 (2005).
2. Mallick, K. *et al.* Reintroducing radiometric surface temperature into the penman-monteith formulation. *Water Resour. Res.* **51**, 6214–6243 (2015).
3. Timmermans, W. J., Kustas, W. P., Anderson, M. C. & French, A. N. An intercomparison of the surface energy balance algorithm for land (sebal) and the two-source energy balance (tseb) modeling schemes. *Remote. Sens. Environ.* **108**, 369–384 (2007).
4. Mallick, K. *et al.* A critical evaluation on the role of aerodynamic and canopy–surface conductance parameterization in sebal and svat models for simulating evapotranspiration: A case study in the upper biebrza national park wetland in poland. *Water* **10**, 1753 (2018).
5. Trebs, I. *et al.* The role of aerodynamic resistance in thermal remote sensing-based evapotranspiration models. *Remote. Sens. Environ.* **264**, 112602 (2021).
6. Kustas, W. & Anderson, M. Advances in thermal infrared remote sensing for land surface modeling. *Agric. For. Meteorol.* **149**, 2071–2081 (2009).
7. Still, C. J. *et al.* Imaging canopy temperature: shedding (thermal) light on ecosystem processes. *New Phytol.* **230**, 1746–1753 (2021).
8. Mallick, K. *et al.* Bridging thermal infrared sensing and physically-based evapotranspiration modeling: From theoretical implementation to validation across an aridity gradient in australian ecosystems. *Water Resour. Res.* **54**, 3409–3435 (2018).
9. Norman, J. M. & Becker, F. Terminology in thermal infrared remote sensing of natural surfaces. *Agric. For. Meteorol.* **77**, 153–166 (1995).
10. Kustas, W. P., Anderson, M. C., Norman, J. M. & Li, F. Utility of radiometric–aerodynamic temperature relations for heat flux estimation. *Boundary-Layer Meteorol.* **122**, 167–187 (2007).
11. Stoy, P. C. *et al.* A data-driven analysis of energy balance closure across fluxnet research sites: The role of landscape scale heterogeneity. *Agric. forest meteorology* **171**, 137–152 (2013).
12. Cullen, N. J., Mölg, T., Kaser, G., Steffen, K. & Hardy, D. R. Energy-balance model validation on the top of kilimanjaro, tanzania, using eddy covariance data. *Annals Glaciol.* **46**, 227–233 (2007).
13. Baldocchi, D. *et al.* Fluxnet: A new tool to study the temporal and spatial variability of ecosystem-scale carbon dioxide, water vapor, and energy flux densities. *Bull. Am. Meteorol. Soc.* **82**, 2415–2434 (2001).
14. Guillevic, P. *et al.* Land surface temperature product validation best practice protocol. version 1.0. *Best Pract. for Satell. Land Prod. Valid.* 60 (2017).
15. Wang, K. & Dickinson, R. E. Global atmospheric downward longwave radiation at the surface from ground-based observations, satellite retrievals, and reanalyses: DOWNWARD LONGWAVE RADIATION. *Rev. Geophys.* **51**, 150–185, DOI: [10.1002/rog.20009](https://doi.org/10.1002/rog.20009) (2013).
16. Sun, J. & Mahrt, L. Relationship of surface heat flux to microscale temperature variations: Application to boreas. *Boundary-Layer Meteorol.* **76**, 291–301 (1995).
17. Jacob, D. *et al.* A comprehensive model inter-comparison study investigating the water budget during the baltex-pidcap period. *Meteorol. Atmospheric Phys.* **77**, 19–43 (2001).
18. Mallick, K. *et al.* Canopy-scale biophysical controls of transpiration and evaporation in the amazon basin. *Hydrol. Earth Syst. Sci.* **20**, 4237–4264 (2016).
19. Lhomme, J.-P., Katerji, N., Perrier, A. & Bertolini, J.-M. Radiative surface temperature and convective flux calculation over crop canopies. *Boundary-Layer Meteorol.* **43**, 383–392, DOI: [10.1007/BF00121714](https://doi.org/10.1007/BF00121714) (1988).



20. Holmes, T. R. H., Jeu, R. A. M. D., Owe, M. & Dolman, A. J. Land surface temperature from Ka band (37 GHz) passive microwave observations. *J. Geophys. Res. Atmospheres* **114**, DOI: [10.1029/2008JD010257](https://doi.org/10.1029/2008JD010257) (2009).
21. Holmes, T. R. H., Hain, C. R., Anderson, M. C. & Crow, W. T. Cloud tolerance of remote-sensing technologies to measure land surfacetemperature. *Hydrol. Earth Syst. Sci.* **20**, 3263–3275, DOI: [10.5194/hess-20-3263-2016](https://doi.org/10.5194/hess-20-3263-2016) (2016).
22. Maes, W. H., Gentine, P., Verhoest, N. E. & Miralles, D. G. Potential evaporation at eddy-covariance sites across the globe. *Hydrol. Earth Syst. Sci.* **23**, 925–948 (2019).
23. Chu, H. *et al.* Representativeness of eddy-covariance flux footprints for areas surrounding ameriflux sites. *Agric. For. Meteorol.* **301**, 108350 (2021).
24. Marcolla, B. & Cescatti, A. Geometry of the hemispherical radiometric footprint over plant canopies. *Theor. Appl. Climatol.* **134**, 981–990 (2018).
25. Morillas, L. *et al.* Using radiometric surface temperature for surface energy flux estimation in mediterranean drylands from a two-source perspective. *Remote. Sens. Environ.* **136**, 234–246 (2013).
26. Wang, K. & Liang, S. Evaluation of ASTER and MODIS land surface temperature and emissivity products using long-term surface longwave radiation observations at SURFRAD sites. *Remote. Sens. Environ.* **113**, 1556–1565, DOI: [10.1016/j.rse.2009.03.009](https://doi.org/10.1016/j.rse.2009.03.009) (2009).
27. Trenberth, K. E. & Fasullo, J. T. Tracking earth's energy: From el niño to global warming. *Surv. geophysics* **33**, 413–426 (2012).
28. Crago, R. D. & Qualls, R. J. Use of land surface temperature to estimate surface energy fluxes: Contributions of Wilfried Brutsaert and collaborators. *Water Resour. Res.* **50**, 3396–3408, DOI: [10.1002/2013WR015223](https://doi.org/10.1002/2013WR015223) (2014).
29. Stephens, G. L. Review of atmospheric radiation: 1991–1994. *Rev. Geophys.* **33**, 785–794 (1995).
30. Crago, R. D. & Qualls, R. J. Use of land surface temperature to estimate surface energy fluxes: Contributions of Wilfried Brutsaert and collaborators. *Water Resour. Res.* **50**, 3396–3408, DOI: [10.1002/2013WR015223](https://doi.org/10.1002/2013WR015223) (2014).
31. Rosolem, R., Gupta, H. V., Shuttleworth, W. J., Zeng, X. & De Gonçalves, L. G. G. A fully multiple-criteria implementation of the sobol' method for parameter sensitivity analysis. *J. Geophys. Res. Atmospheres* **117** (2012).
32. Holmes, T. R. H., Hain, C. R., Anderson, M. C. & Crow, W. T. Cloud tolerance of remote-sensing technologies to measure land surfacetemperature. *Hydrol. Earth Syst. Sci.* **20**, 3263–3275, DOI: [10.5194/hess-20-3263-2016](https://doi.org/10.5194/hess-20-3263-2016) (2016).
33. Sugita, M. & Brutsaert, W. Optimal Measurement Strategy for Surface Temperature to Determine Sensible Heat Flux From Anisothermal Vegetation. *Water Resour. Res.* **32**, 2129–2134, DOI: [10.1029/96WR00993](https://doi.org/10.1029/96WR00993) (1996).
34. Snyder, W. C., Wan, Z., Zhang, Y. & Feng, Y.-Z. Classification-based emissivity for land surface temperature measurement from space. *Int. J. Remote. Sens.* **19**, 2753–2774 (1998).
35. Holmes, T. R. H., Jeu, R. A. M. D., Owe, M. & Dolman, A. J. Land surface temperature from Ka band (37 GHz) passive microwave observations. *J. Geophys. Res. Atmospheres* **114**, DOI: [10.1029/2008JD010257](https://doi.org/10.1029/2008JD010257) (2009).
36. Wilson, K. *et al.* Energy balance closure at fluxnet sites. *Agric. For. Meteorol.* **113**, 223–243 (2002).
37. Foken, T. The energy balance closure problem: an overview. *Ecol. Appl.* **18**, 1351–1367 (2008).
38. Chen, Y., Sun-Mack, S., Minnis, P., Smith, W. L. & Young, D. F. Surface spectral emissivity derived from modis data. In *Optical Remote Sensing of the Atmosphere and Clouds III*, vol. 4891, 361–369 (International Society for Optics and Photonics, 2003).
39. Juang, J.-Y., Katul, G., Siqueira, M., Stoy, P. & Novick, K. Separating the effects of albedo from eco-physiological changes on surface temperature along a successional chronosequence in the southeastern united states. *Geophys. Res. Lett.* **34** (2007).
40. Guillevic, P. *et al.* Land surface temperature product validation best practice protocol. version 1.1. *Best Pract. for Satell. Land Prod. Valid.* 60 (2018).
41. Jin, M. & Liang, S. An Improved Land Surface Emissivity Parameter for Land Surface Models Using Global Remote Sensing Observations. *J. Clim.* **19**, 2867–2881, DOI: [10.1175/JCLI3720.1](https://doi.org/10.1175/JCLI3720.1) (2006).
42. Mira, M., Valor, E., Boluda, R., Caselles, V. & Coll, C. Influence of soil water content on the thermal infrared emissivity of bare soils: Implication for land surface temperature determination. *J. Geophys. Res. Earth Surf.* **112** (2007).
43. Chen, C. Determining the leaf emissivity of three crops by infrared thermometry. *Sensors* **15**, 11387–11401 (2015).

44. Vishnevetsky, I., Rotenberg, E., Kribus, A. & Yakir, D. Method for accurate measurement of infrared emissivity for opaque low-reflectance materials. *Appl. optics* **58**, 4599–4609 (2019).
45. Eisenhauer, J. G. Regression through the origin. *Teach. statistics* **25**, 76–80 (2003).
46. Gilberto, P. *et al.* The fluxnet2015 dataset and the oneflux processing pipeline for eddy covariance data. *Sci. Data* (2020).
47. Wan, Z. Collection-5 modis land surface temperature products users' guide. *ICESSE, Univ. California, Santa Barbar.* (2007).
48. Delucchi, L. pymodis: from satellite to gis maps. In *FOSS4G 2014* (2014).
49. Wang, K. Estimation of surface long wave radiation and broadband emissivity using Moderate Resolution Imaging Spectroradiometer (MODIS) land surface temperature/emissivity products. *J. Geophys. Res.* **110**, D11109, DOI: [10.1029/2004JD005566](https://doi.org/10.1029/2004JD005566) (2005).
50. Hulley, G. C., Hughes, C. G. & Hook, S. J. Quantifying uncertainties in land surface temperature and emissivity retrievals from ASTER and MODIS thermal infrared data. *J. Geophys. Res. Atmospheres* **117**, DOI: [10.1029/2012JD018506](https://doi.org/10.1029/2012JD018506) (2012).
51. Jin, M. & Liang, S. An improved land surface emissivity parameter for land surface models using global remote sensing observations. *J. Clim.* **19**, 2867–2881 (2006).
52. Wang, K. & Liang, S. Evaluation of ASTER and MODIS land surface temperature and emissivity products using long-term surface longwave radiation observations at SURFRAD sites. *Remote. Sens. Environ.* **113**, 1556–1565, DOI: [10.1016/j.rse.2009.03.009](https://doi.org/10.1016/j.rse.2009.03.009) (2009).
53. Bahir, M. *et al.* Evaluation and Aggregation Properties of Thermal Infra-Red-Based Evapotranspiration Algorithms from 100 m to the km Scale over a Semi-Arid Irrigated Agricultural Area. *Remote. Sens.* **9**, 1178, DOI: [10.3390/rs9111178](https://doi.org/10.3390/rs9111178) (2017).
54. Rannik, Ü., Peltola, O., Mammarella, I. *et al.* Random uncertainties of flux measurements by the eddy covariance technique. *Atmospheric Meas. Tech.* (2016).
55. Mauder, M., Foken, T. & Cuxart, J. Surface-energy-balance closure over land: a review. *Boundary-Layer Meteorol.* **177**, 395–426 (2020).
56. Vickers, D., Göckede, M. & Law, B. Uncertainty estimates for 1-h averaged turbulence fluxes of carbon dioxide, latent heat and sensible heat. *Tellus B: Chem. Phys. Meteorol.* **62**, 87–99 (2010).
57. Saltelli, A., Albrecht, D., Tarantola, S. & Ferretti, F. A new sample-based algorithms to compute the total sensitivity index. *arXiv preprint arXiv:1703.05799* (2017).
58. Jin, M. & Liang, S. An Improved Land Surface Emissivity Parameter for Land Surface Models Using Global Remote Sensing Observations. *J. Clim.* **19**, 2867–2881, DOI: [10.1175/JCLI3720.1](https://doi.org/10.1175/JCLI3720.1) (2006).

## 5 Supplementary Information

### SI1. Abbreviation list

### SI2. Comparison table of plot-scale LST with landscape LST using landscape and plot-scale $\varepsilon$

### SI3. Emissivity estimation at Howards spring and positive $T_s - T_a$

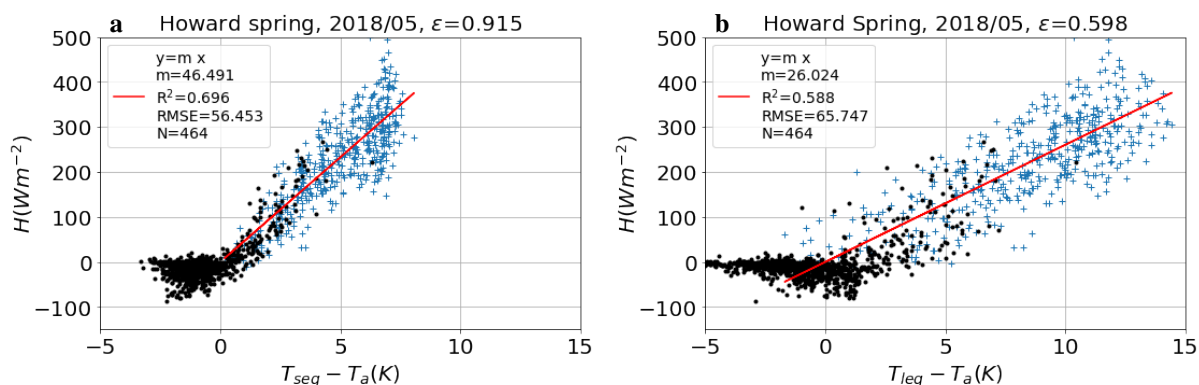


**Figure 8.** *Hand* $\Delta T$  plots at Howards Spring with optimised emissivity

**Table 3.** Abbreviation list

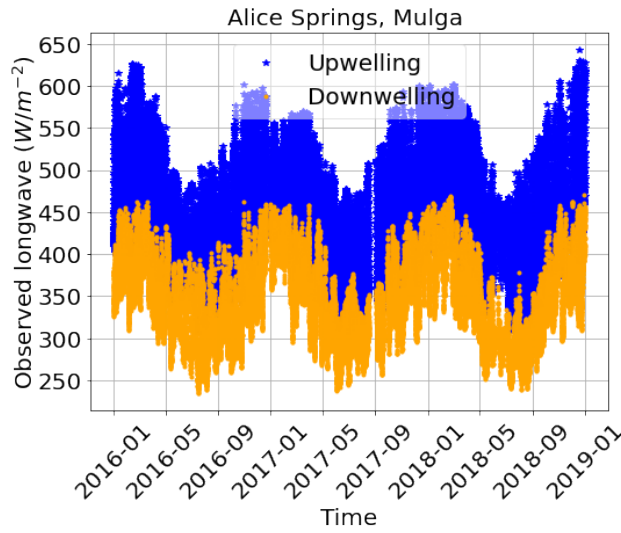
Symbol	Description	Unit
$R_{net}$	Net radiation	$\text{W m}^{-2} \text{ m}$
$H$	Sensible heat flux	$\text{W m}^{-2}$
$LE$	Latent heat flux	$\text{W m}^{-2}$
$G$	Ground heat flux	$\text{W m}^{-2}$
$R_{lem}$	Emitted longwave radiation	$\text{W m}^{-2}$
$\varepsilon$	Surface emissivity	(-)
$\sigma$	Stefan-Boltzmann constant	$\text{W m}^{-2} \text{K}^{-4}$
$T_s$	Surface temperature	K
$R_{sdown}$	Down-welling shortwave	$\text{W m}^{-2}$
$R_{ldown}$	Down-welling longwave	$\text{W m}^{-2}$
$R_{sref}$	Reflected shortwave	$\text{W m}^{-2}$
$\alpha$	Surface albedo	(-)
$m$	Aerodynamic conductance to heat transport	( $\text{m/s}$ )
$\varepsilon_{31}$	Spectral emissivity for wavelength of $11 \mu\text{m}$	(-)
$\varepsilon_{32}$	Spectral emissivity for wavelength of $12 \mu\text{m}$	(-)
BADAM	Ameriflux dataset	(-)
TERRA	NASA scientific research satellite	(-)
NATT	North Australian Tropical Transect	(-)

Sites	Landscape-scale $\varepsilon$						Plot-scale $\varepsilon$					
	$\varepsilon$	seq		leq			seq			leq		
		$R^2$	bias	$R^2$	bias		opt $\varepsilon$	$R^2$	bias	opt $\varepsilon$	$R^2$	bias
SP	0.974	0.80	-3.67	0.81	-4.61		0.96	0.81	-3.0	0.85	0.82	-1.91
AS	0.974	0.93	-4.78	0.93	-6.31		0.96	0.93	-3.4	0.82	0.93	-1.92
TT	0.974	0.55	-6.76	0.57	-8.30		0.95	0.58	-5.06	0.80	0.52	-4.02
HS	0.985	0.16	-8.89	0.16	-9.90		0.92	0.21	-4.78	0.6	0.22	-2.47
LF	0.985	0.40	-10.0	0.41	-11.0		0.92	0.40	-4.41	0.6	0.41	-2.57
AR	0.985	0.18	-2.61	0.27	-3.51		0.997	0.23	-2.93	0.96	0.252	-2.98
DU	0.985	0.80	-3.67	0.81	-4.61		0.99	0.428	-3.682	0.985	0.425	-3.926
TUM	0.983	0.82	-2.27	0.84	-2.10		0.99	0.89	0.99	0.97	0.89	1.93
BR	0.983	0.937	0.525	0.937	-0.195		0.98	0.917	1.87	0.82	0.895	2.72
YA	0.974	0.855	-2.081	0.855	-3.45		0.97	0.522	-4.517	0.93	0.793	-0.582

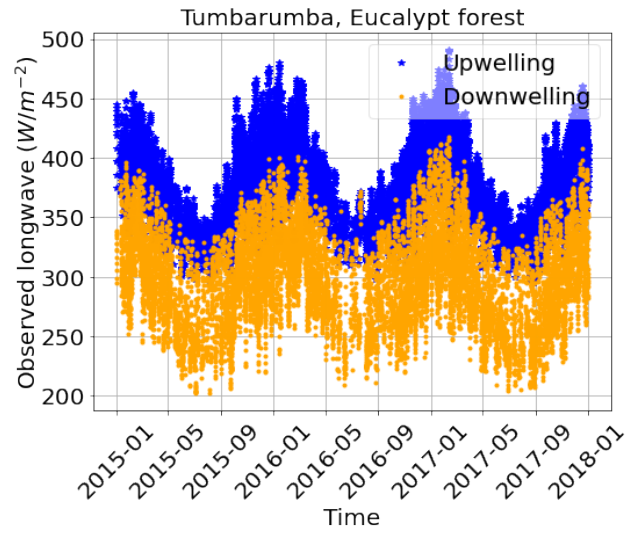
**Table 4.** Comparison of plot-scale LST with landscape-scale daytime LST (MODIS, MODA001) at TERRA daily time of pass. Plot scale LST is obtained using landscape-scale emissivity (MODIS  $\varepsilon$ ) and plot-scale emissivity (Optimum  $\varepsilon$ ) at study sites. The reported plot-scale emissivity are median values and landscape emissivity are MODIS based. Bias is defined as mean of  $T_s - T_{MODIS}$ ,  $R^2$  is coefficient of determination between plot-scale LST in comparison to landscape-scale LST. The site acronyms can be found in Table 2

#### SI4. $T_s$ sensitivity to $\varepsilon$ at Alice spring and Tumbarumba

In general, the broadband emissivity range for a land cover can vary between 0.87 to 0.98<sup>58</sup>. The noontime measured longwave for two contrasting landcover types (semi-arid mulga, tropical savanna woodland) are used to quantify the sensitivity of LST to emissivity as shown in Fig. (10).

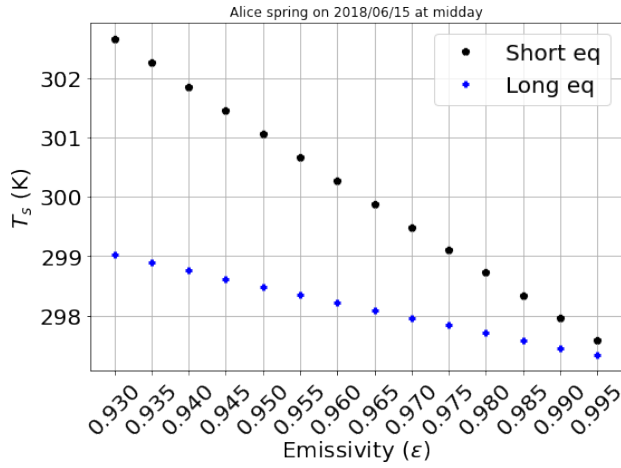


(a) Alice Springs

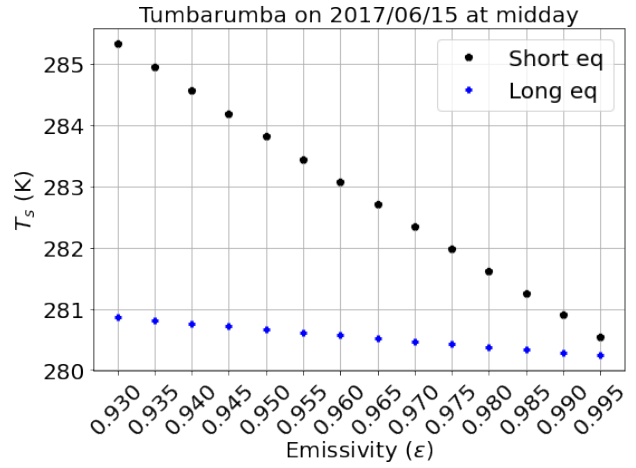


(b) Tumbarumba

**Figure 9.** Measured up-welling and down-welling longwave timeseries



(a)



(b)

**Figure 10.** Sensitivity of LST estimated using two equations to the range of Broadband emissivity The black dots and blue Stars depicts LST using simplified (Eq. 11) and complete (Eq. (6)). Midday longwave measurement for 15June, 2016 at Alice Springs and Tumbarumba is used

**SI5.RMSE and Epsilon**

**SI6.Energy imbalance and observed fluxes**

**SI7.H and intercept**

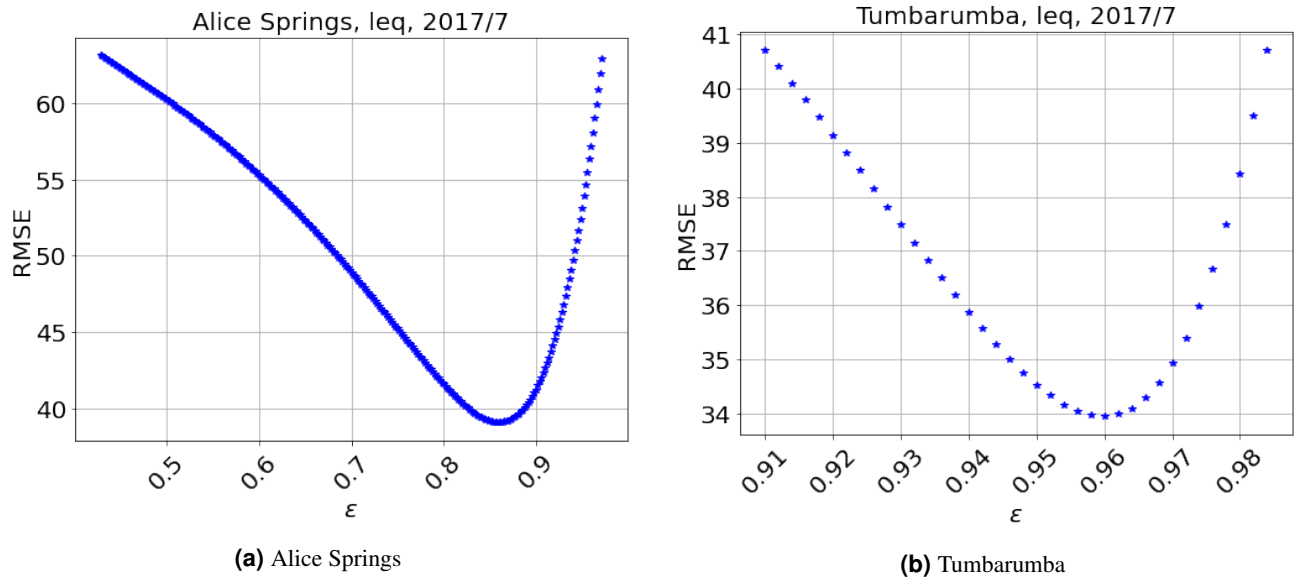


**Figure 11.** RMSE and emissivity curve

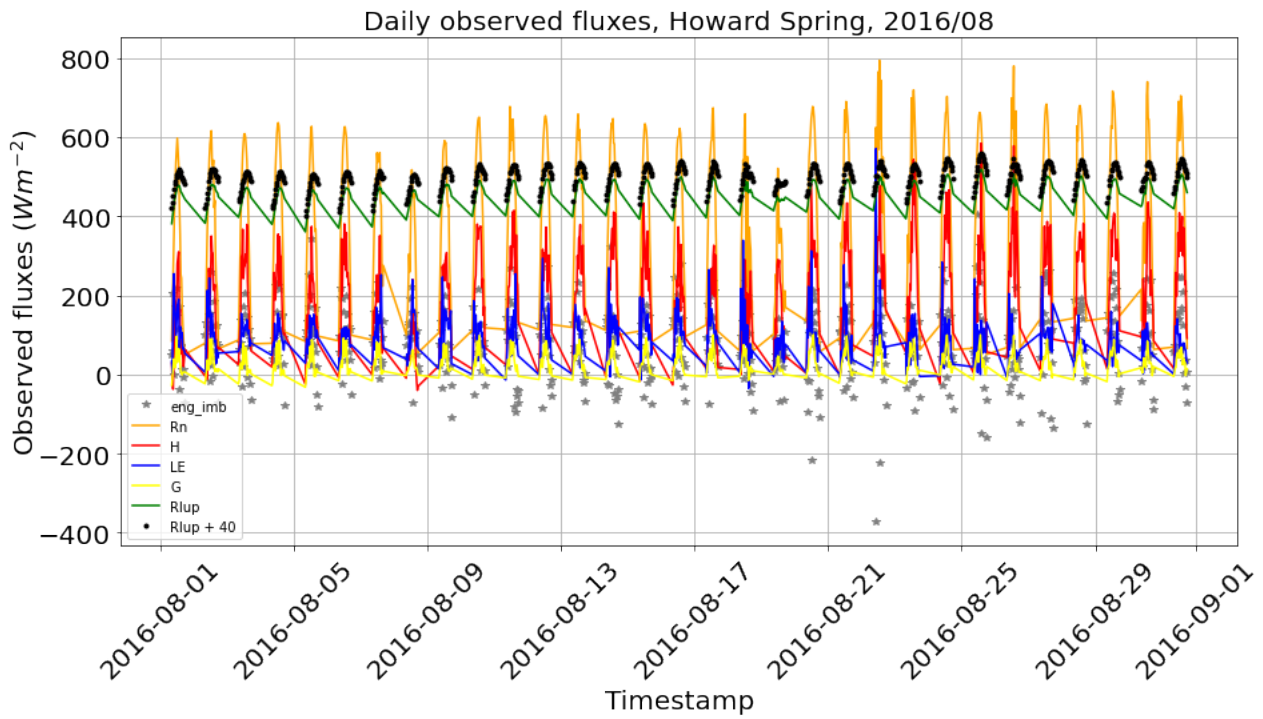


**Figure 12.** Measured fluxes and estimated energy imbalance at Howard springs for 2016/08



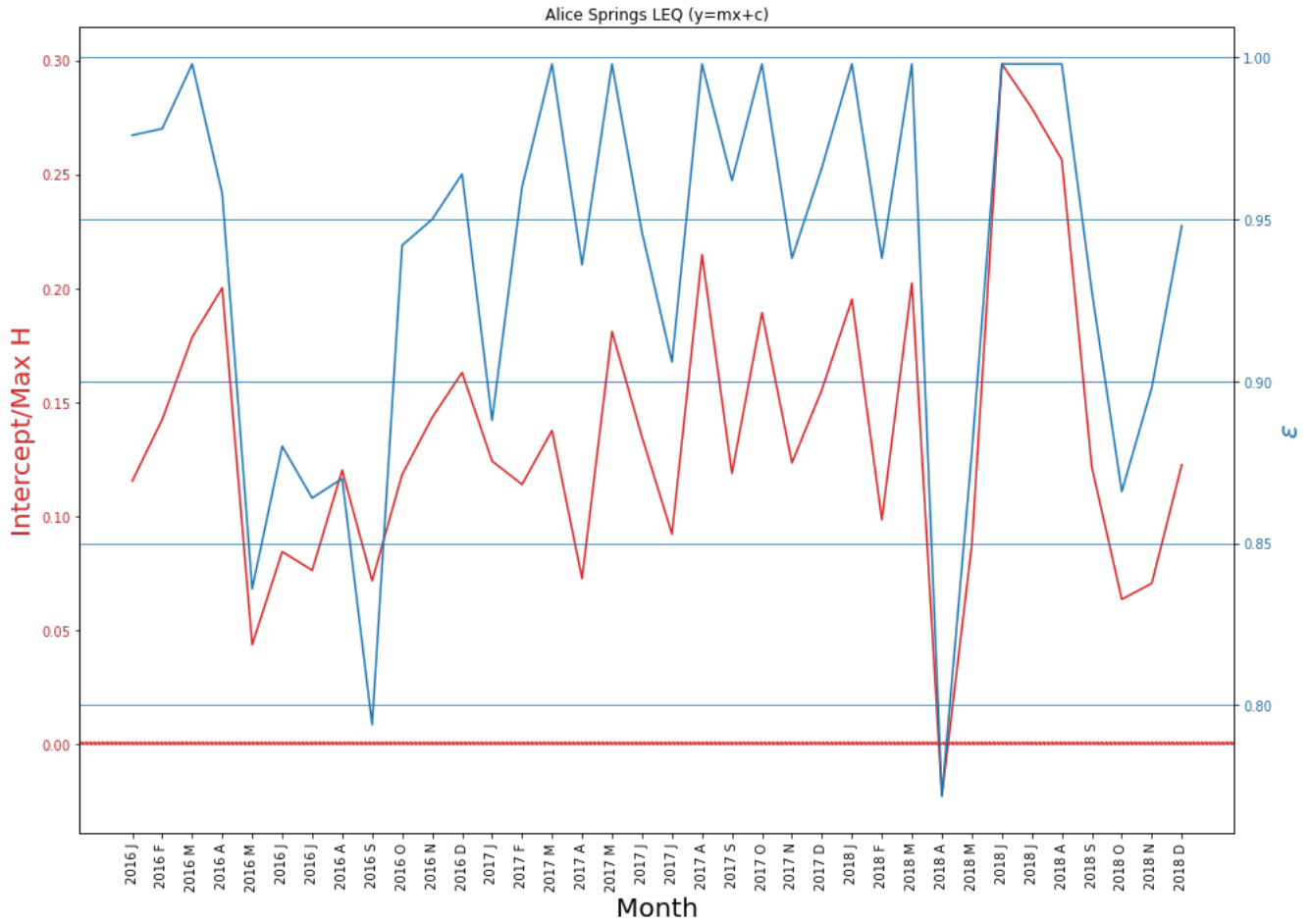


**Figure 13.** Monthly  $H \Delta T$  plots showing offset at  $\Delta T=0$  (a) using simplified equation (Eq. 11). (b) using complete equation (Eq. 6)(c). Estimated intercept (c) for each month using  $H = m(T_s - T_a) + c$ . Red line is intercept and blue line shows monthly  $\epsilon$  obtained by minimising RMSE at Alice Springs (2016 - 2018).